Database Of Simulated Inverse Synthetic Aperture Radar Images For Short Range Automotive Radar

Neeraj Pandey, Gaurav Duggal and Shobha Sundar Ram
Indraprastha Institute of Information Technology Delhi, New Delhi 110020 India
E-mail: {neerajp, gaurav17091, shobha}@iiitd.ac.in

Abstract—Inverse synthetic aperture radar (ISAR) images of dynamic targets have been used for automatic target recognition purposes. Limited experimental data of ISAR images of automotive targets are currently available to the radar community. In this paper, we propose an electromagnetic simulation model for generating ISAR images of dynamic automotive targets for a short-range automotive radar. Further, we provide an open-source database of approximately 750 ISAR images for each of five common automotive targets - two cars, truck, bicycle, and auto-rickshaw. Our results show that ISAR images provide useful insights regarding the dimensions of the vehicles, the number of wheels and the orientation of the vehicle along its trajectory with respect to the radar.

Index Terms—automotive radar, ISAR, open source database, short range radar

I. Introduction

There has been significant research on developing advanced driver assistance systems (ADAS) for avoiding road accidents, reducing road fatalities, and eventually facilitating autonomous or self-driving vehicles [1]. The challenge in these systems is to detect and recognize the automotive targets. The ego vehicle may use sensors such as lidar, camera, infrared/thermal detectors, and radar to detect other road users. Radars are capable of both range and velocity estimation, 24x7 detection, and operation in adverse conditions such as rain, fog, and snow. Further, radars can be mounted behind the front and rear bumper fascia for maintaining vehicle aesthetics [2]. In this paper, we propose a method to generate radar images of common automotive targets such as bicycles, cars, and trucks to create a database for facilitating automatic target recognition (ATR). This will enable important functionalities in the ADAS systems such as lane change assistance and rear and forward cross-traffic alert.

Inverse synthetic aperture radar (ISAR) is a well-established technique for high-resolution radar imaging of moving objects [3]–[6]. ISAR images have been extensively researched for airborne, spaceborne and waterborne targets for facilitating ATR [7]–[10]. The traditional arrangement of ISAR is to consider a stationary monostatic broadband radar and a dynamic target undergoing rotational motion. The large bandwidth enables fine downrange resolution, and the rotational motion provides the radar with a large synthetic aperture for obtaining fine cross-range resolution. The advantage of ISAR is that high-resolution images of targets are realized with single-channel sensor data without the requirement of costly and complex hardware with large antenna arrays with lots of elements and receiver channels.

Currently, there is growing interest in ISAR imaging of ground moving vehicles, especially at automotive radar frequencies. ISAR imaging of ground moving vehicles with a stationary radar was realized with experimental data in [11]–[13] and high-resolution ISAR imaging of a car was carried out by capturing turntable measurement data in [14], ISAR images of ground vehicles were realized with airborne sensors in [15]–[19]. In all of the above works, the ISAR images were generated for a few automotive targets under controlled laboratory conditions. However, these limited data sets are not available to the radar community and not sufficient for supporting state-of-art target recognition algorithms. Of late, the radar community has been increasingly turning to learning algorithms based on deep convolutional neural networks (DCNN) for ATR [20]–[23]. In multiple applications, these algorithms have demonstrated their superiority in terms of feature extraction and classification performance, especially with respect to traditional approaches of heuristic parameter selection for machine learning-based target recognition. However, the performance of DCNNs relies on the availability of large training databases gathered in diverse scenarios. The data set must comprise of different types of automotive targets such as vehicles of diverse sizes, moving along different trajectories and orientations with respect to radar. Similarly, there must be diversity in the road conditions in terms of clutter and interference. There are two possible methods for generating training data sets. The first method is to collect the data in real traffic and target scenarios using actual automotive radar sensors. The advantage is that the training data is realistic and can be gathered both in laboratory conditions and during test drives. However, the disadvantage is that the task of data collection and labelling is both time-consuming and laborious. Further, the database must be updated based on hardware modifications to the sensor or due to software upgrades to the signal processing. Also, the captured data may be corrupted in the presence of clutter in the environment and by hardware limitations of the sensor. The second method to generate a large volume of training data is to simulate the sensor, target, and traffic conditions. The advantage of simulation is that the training data set can be generated rapidly for the diverse sensor, channel, and target conditions. Also, the simulator can be easily integrated with the radar test-bed and signal processing platforms for rapid prototyping and validations. Finally, the simulator can be useful to study the effects of different radar phenomenology, including sensor position and parameters, clutter, and road conditions on the radar signatures.

In this paper, we provide two main contributions: First, we propose a realistic electromagnetic radar signal model for generating ISAR images of different types of targets; Second, we provide an open-source database of ISAR radar images of five common automotive targets carrying out diverse motions along different trajectories. We consider a short-range automotive radar mounted on a stationary platform near a four-way traffic junction. We consider five automotive targets - two types of cars, a truck, an auto-rickshaw, and a bicycle - and four types of motions for each target. The motions are right turn, left turn, U-turn, and straight path. For each of the four motion categories, we consider four possible trajectories based on the four paths in the junction. For example, the right turn may take place from south to east, east to north, north to west, and west to south. We obtain a computer animation model of each of the targets and render the metal chassis of each into several hundred triangular facets. Then we animate each target along a desired trajectory using Euler based rotation operations and translational operations. We consider a

238

linear frequency modulated transmitted signal with radar parameters comparable to existing commercial automotive short-range radars [1]. Then, we simulate the radar scattered returns from the vehicle by the complex sum of the returns from point scatterers located at the center of each of the facets on the body of the vehicle. This type of scattering center-based modeling is computationally simple and quick to execute, especially in comparison to full-wave electromagnetic solvers. They are especially useful for modeling returns of dynamic targets. [24], [25]. The received radar returns are *stretch* processed along the fast time dimension to obtain range, and Fourier processed along the slow time dimension to obtain Doppler information. Based on the knowledge of the target trajectory, we perform translational motion compensation. Therefore, the Doppler returns are a function of the rotational motion of the point scatterers on the vehicles during turns. Using angular velocity estimates of the vehicle's turning motion, we convert the range-Doppler ambiguity plots to range-cross ISAR maps for each coherent processing interval of the radar data. The ISAR images for all the targets and their trajectories for different motions are provided to the radar community in https://tinyurl.com/tdy7kog.

The paper is organized as follows. In the following section, we present the simulation methodology for generating electromagnetic radar returns from dynamic automotive targets. In Section III, we present the method for obtaining ISAR images based on the stretch processing of the radar data. In Section IV, we present some examples of the ISAR images for the different targets, their motions, and trajectories. Finally, we present a discussion on the results in the concluding section.

II. SIMULATION METHODOLOGY

In this section, we present the detailed simulation model of radar scattered returns from five automotive targets. The five targets that we have considered are a full-sized car, a mid-sized car, a bicycle, truck, and an auto-rickshaw. The make and model of each of the targets are presented in Table.I. We obtain a computer aided design (CAD)

TABLE I: Description of Automotive Targets

Vehicle Type	Make and Model	Number of facets
Full sized car	BMW M5	19964
Mid sized car	Vauxhall Astra VXR	6905
Bicycle	Urban Terrain UT1000	3919
Auto-rickshaw	Standard	6949
Truck	TATA motors TATA 1512	7206

model of each of the targets [2] and render the metallic portion of the CAD models into triangular facets as shown in Fig.1. The number of facets for each of the targets is mentioned in the table. We consider a road geometry as shown in Fig.2a. The scenario is a traffic junction where four roads from north, south, east, and west meet. We assume that all the targets are standing on the xy ground plane with the height along the z axis. The x axis is assumed to be oriented along north-south while the y axis is along east-west. We assume that the radar is fixed and is positioned at $\vec{r}_{rad} = (0,0,0.5)m$ as indicated in Fig.2a. Each of the roads allows for bi-directional traffic with two lanes each for each direction of traffic. Each lane is $3.75m$ in width. An additional lane of $3.5m$ is carved out near the junction in each road to facilitate right turns. Each of the five targets can perform any of four different motions at the junction. The vehicle can turn right,

turn left, perform a U-turn, or go straight, as shown in Fig.2b. Each of these motion categories can be conducted along any of the four trajectories. For example, a right turn can be from the south to east, east to north, north to west, and west to south. Similarly, a straight path can be from the south to north, north to south, east to west and west to east.

We animate each target along a specified trajectory. Each vehicle undergoes a combination of translational and rotational motions. We divide the duration of the trajectory into F intervals specified by a video frame rate $(1/t_f)$. Then, we translate the center of gravity (CG) of the vehicle $(\vec{r}_{CG} = (x_{CG}, y_{CG}, z_{CG}))$ along the trajectory. Since, the vehicle is a rigid body, the displacement of the vertices of each facet $\vec{\Delta r_i}$ with respect to the CG is fixed. Therefore, the position of the center of the facet at any frame f is $\vec{r}_i[f] = \vec{r}_i[f] + \vec{\Delta r_i}$. In order to incorporate the rotational motion, we compute the required yaw (rotation about the positive z axis, $\theta[f]$) of the vehicle for each f frame on the basis of the change in the $x_{CG}[f]$ and $y_{CG}[f]$. Then we rotate the facet through Euler based rotation operations on the vertices. We further incorporate wheel dynamics in the model. The center of each wheel moves with the velocity of the vehicle. Therefore, the angular displacement $(\alpha[f])$ of any point on the rim of the wheel over t_f can be computed from the ratio of the translational distance moved by the vehicle in a t_f to the radius of the wheel. We then perform a second Euler based rotation operation for every $\alpha[f]$ on these points to model the rotational motion of each wheel. If we assume that each of the triangular facets is an independent scatterer, then the radar cross-section of any b^{th} facet for a wavelength λ is given by

$$\sigma_b = \frac{4\pi A_b^2 \cos^2 \theta_b}{\lambda^2} \frac{\sin^4 \left(\frac{2\pi}{\lambda} d_b \sin \theta_b \right)}{\left(\frac{2\pi}{\lambda} d_b \sin \theta_b \right)^4}, \tag{1}$$

where A_b is the area of the triangle, and θ_b and d_b are the aspect angle and the dimension of the plate along the aspect of the triangle with respect to the radar respectively [26]. The aspect angle is computed from the dot product of the incident vector from the radar to the plate and the normal vector of the plate. Since, the facets are metallic, they are assumed to be perfectly reflecting. If we ignore multipath scattering, then the amplitude of the direct return signal from the scattering center of the triangle is $a_b = \sqrt{\sigma_b}/r_b^2$. As the target moves along the trajectory, the aspect angle and the distance of the facet from the radar change resulting in fluctuations in the scattering amplitude.

III. ISAR IMAGING USING STRETCH PROCESSING

The transmitted radar signal is a linear frequency modulated waveform with a carrier frequency of Ω and a chirp rate γ. The transmitted signal is given by

$$s_{tx}(\tau) = rect \left(\frac{\tau}{T_{PRI}} \right) e^{j\Omega\tau} e^{j\pi\gamma\tau^2}, \tag{2}$$

where the chirp duration is equal to T_{PRI} which is the pulse repetition interval (PRI) and

$$rect \left(\frac{\tau}{T_{PRI}} \right) = \begin{cases} 1 & 0 \leq \tau \leq T_{PRI} \\ 0 & \text{elsewhere.} \end{cases} \tag{3}$$

If we consider a point scatterer, b, of scattering amplitude a_b, at downrange distance r_b from the radar, then the time delay of the radar signal over the direct path is $\frac{2r_b(t)}{c}$. Here $\frac{2r_b(t)}{c}$ varies over the slow time t across several PRIs constituting a coherent processing interval (CPI). The received radar signal from the point scatterer over a CPI can be expressed as a two-dimensional function of fast time (τ) within one PRI and slow time (t) as shown as

$$s_{rx}(\tau, t) = a_b rect \left(\frac{\tau - \frac{2r_b(t)}{c}}{T_{PRI}} \right) e^{-j\Omega \frac{2r_b(t)}{c}} e^{j\pi\gamma \left(\tau - \frac{2r_b(t)}{c} \right)^2}. \tag{4}$$
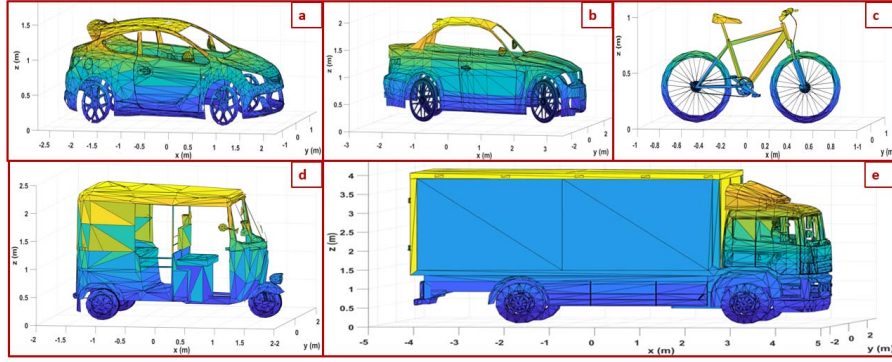
239

Fig. 1: Three-dimensional rendering of metallic chassis and wheels of automotive targets with triangular facets. (a) Mid-sized car is rendered with 6905 triangles, (b) full-sized car is rendered with 19964 triangles, (c) bicycle is rendered with 3919 triangles, (d) auto-rickshaw (tuk-tuk) is rendered with 6949 triangles and (e) full-sized truck is rendered with 7206 triangles.
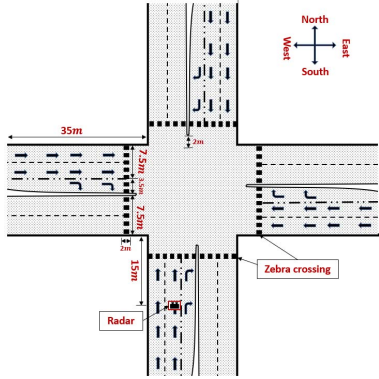
(a) Road geometry of four-way traffic junction
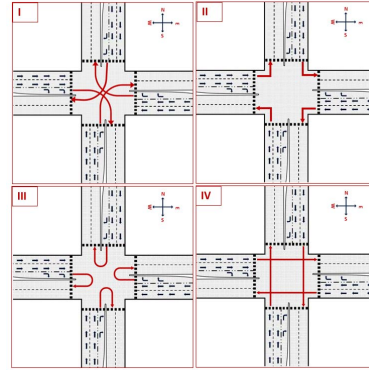
(b) (i)Right turn, (ii) Left turn, (iii) U-turn and (iv) Straight

Fig. 2: Motions trajectories that vehicles can undertake in a four-way traffic junction. Short-range automotive radar is situated at (0,0,0.5)m along the south road.

Note that in the above expression, we have assumed that the received signal has been downconverted to the baseband.

LFM signals are usually processed with matched filtering along the fast time dimension resulting in a maximum unambiguous range of $R_{max} = \frac{cT_{PRI}}{2}$. In stretch processing, however, we consider a central reference position R_0 at the center of the range window of interest in every CPI. The time delay to R_0 is $\tau_0 = \frac{2R_0}{c}$. The time delay to the point scatterer, b, can be expressed as $\frac{2r_b(t)}{c} = \tau_0 + \delta\tau_b(t)$. The received signal is processed with $e^{-j\pi\gamma(\tau-\tau_0)^2}$, over every PRI to obtain

$$y_b(\tau, t) = a_b e^{-j\Omega\frac{2R_b}{c}} e^{+j\pi\gamma(\delta\tau_b)^2} e^{-j2\pi\gamma\tau_0\delta\tau_b} \times$$
$$e^{-j2\pi f_{D_b}t} e^{-j2\pi\gamma\delta\tau_b\tau}. \qquad (5)$$

Here R_b is the starting position of the point scatterer in every CPI and f_{D_b} is the Doppler frequency, proportional to Ω, that arises from the motion of the point scatterer. The point scatterer may undergo a combination of rotational and translational motions. However, we only consider the rotational motion of the point scatterer and intentionally suppress the translational motion within a CPI. The first three exponential terms in (5) are constant phase terms and are absorbed into the amplitude term during further processing. The last two terms show the variation of the two-dimensional signal over slow and fast times.

When the target is an extended target with multiple point scatterers (B), then the received signal is obtained by the sum of the returns from each scatterer. Since the target motion is known, the central reference point (CRP) is chosen to correspond to the center of the range extent of the target scatterers. The translational motion of all the point scatterers on the target are suppressed by fixing the position of the center of the target for each CPI. The discrete form of the two-dimensional returns can be written as

$$Y[n, p] = \sum_{b=1}^{B} a_b(\cdot) e^{-j2\pi f_{D_b}pT_{PRI}} e^{-j2\pi\gamma\delta\tau_b nT_{SBW}}, \qquad (6)$$

where the slow time $t = [0 \cdots P - 1]T_{PRI}$ and fast time $\tau = [0 \cdots N - 1]T_{SBW}$. The fast time sampling frequency F_s is obtained from twice the stretch bandwidth ($\frac{1}{T_{SBW}}$) which is $\frac{2R_{span}\gamma}{c}$. R_{span} is the span of the range window of interest and is much lower than the maximum unambiguous range of the radar (R_{max}) and c is the speed of light. Note that the sampling frequency required for stretch processing is much lower than what is required for ordinary match filtering where the sampling frequency is usually twice the bandwidth of the transmitted signal ($\gamma T_{PRI} = \frac{2R_{max}\gamma}{c}$). The output of the stretch processor, $Y[n, p]$, is processed using two-dimensional Fourier transform to obtain range-Doppler ambiguity plots,

$$\chi[r, f_D] = \mathcal{DFT}_{2D}\{Y[n, p]\}, \qquad (7)$$

where the range dimension r spans N steps from $R_0 - \frac{R_{span}}{2}$ to $R_0 + \frac{R_{span}}{2}$. The Doppler dimension (f_D) spans P steps from $-\frac{1}{2T_{PRI}}$ to $\frac{1}{2T_{PRI}}$. For each lth CPI, the R_0 is determined by

$$R_0(l) = ||\vec{r}_{CG}(l) - \vec{r}_{rad}||_2^2, \qquad (8)$$

240

where $\vec{r}_{CG}[l] = (x_{CG}[l], y_{CG}[l], z_{CG}[l])$ is the position of center of gravity of the vehicle at the beginning of the CPI and $\vec{r}_{rad}$ is the position of the radar. The Doppler axis for each CPI is converted to the cross range axis by

$$cr[p] = f_D[p] \times \frac{\lambda}{2\omega[l]}, \text{for } p = 0 : P - 1, \qquad (9)$$

where λ corresponds to the wavelength of the carrier frequency of the radar ($\frac{2\pi c}{\Omega}$) and $\omega[l]$ is the angular velocity of the vehicular motion about the Z axis. The angular velocity for each CPI is determined by the change in yaw (Θ) of the vehicle as shown in

$$\omega[l] = \frac{\Theta[l] - \Theta[l-1]}{T_{CPI}}, \qquad (10)$$

where

$$\Theta[l] = \arctan\left(\frac{y_{CG}[l] - y_{CG}[l-1]}{x_{CG}[l] - x_{CG}[l-1]}\right). \qquad (11)$$

Thus the range-Doppler plot provides a range-compensated ISAR image ($\chi[r, cr]$) for each l^{th}CPI. Note that even while the dimensions of the plot remain unchanged for all CPIs, the cross-range spans vary across images depending on $\omega[l]$.

The simulation methodology used for generating ISAR images provides idealized results that may differ from those obtained in real-world conditions in the following ways: *One*, in real-world scenarios, the Doppler frequency f_{D_b} shown in (5) arises from both translational and rotational motions of the target. The Dopplers induced by translational motion gives rise to significant distortions in the ISAR images. Usually, the range of the target's center is estimated from measurements and used for compensating for the translational motion. In our work, since we know the exact trajectory of the target, we are able to suppress the distortions from translational motion completely. We believe that in real-world automotive radars, the estimates of the target range and velocity are fairly accurate and can be used for performing fairly good translational motion compensation. *Two*, incorrect estimation of the angular velocity of the target motion in real-world scenarios can result in distorted ISAR images. Again, in our simulated models, since the target trajectory is exactly known, we are able to estimate the turning velocity accurately. *Three*, in (6), we have performed a complex sum of the radar returns from all the point scatterers on the target. Therefore, all the point scatterers on the target are assumed to be visible to the radar, and effects of shadowing and multiple scattering between the point scatterers have been ignored. Similarly, the effects of system noise and road clutter on the ISAR images have been ignored.

While the vehicles perform gross turning motions such as left turns, right turns and U-turns, their wheels rotate even while the vehicles are moving straight. The micro-motions of the wheels give rise to micro-Dopplers that can significantly distort the ISAR images. In our work, we have retained the wheel dynamics in our models, and hence our images will show the effects of wheel micro-Dopplers on the ISAR images.

IV. EXPERIMENTAL RESULTS

We simulate an automotive radar with parameters that are listed in Table.II. We consider the five automotive targets described in the previous

TABLE II: Radar Parameters

Parameters	Values
Carrier frequency ($\frac{\Omega}{2\pi}$)	77GHz
Stretch Bandwidth ($\frac{1}{T_{SBW}}$)	8MHz
Sampling Frequency (F_s)	16MHz
Chirp rate (γ)	60×10^{12} Hz/sec
Chirp duration (T_{PRI})	$0.83\mu s$
Coherent processing interval (T_{CPI})	0.1s
Range window (R_{span})	20m
Transmitted power	0dBm

section - full-size car, mid-size car, bicycle, auto-rickshaw, and truck. The resulting range and minimum cross-range resolution in the ISAR images are 0.075×0.19m, respectively. For each of the targets, we consider four motions and 4 possible trajectories for each motion. The duration of each motion is 5s. The CPI for the ISAR imaging is set at 0.1s in order to obtain a Doppler resolution of 10Hz. Since we estimate the angular velocity of a target based on the change in yaw of the vehicle over two consecutive CPIs, we do not perform ISAR imaging on the very first CPI, and for that CPI where ω values are less than 0.01 rad/sec. This results in approximately 45 to 49 images for each trajectory of the motion category of a target. Thus, we generate a database of approximately 750 images for each target. All of the images are available in https://tinyurl.com/tdy7kog We show some examples of the simulated ISAR images in Fig.3 through to Fig.7. In all of the figures, the top row shows the ISAR images generated when the vehicle executes a right turn from west to south; the second row shows the results for a vehicle executing a left turn from north to east; the third row shows the results for a U-turn along the south road and the bottom-most row shows the results for a vehicle traveling along a straight path from east to west. The results are shown for four different CPIs at 1s, 2s, 3s, and 4s. The range span in all the figures is 20m, while the cross-range span varies from approximately 10m to 20m. In all of the figures, the strength is normalized to the maximum, and the dynamic range is set at 20dB.

Full-size Car: First, we consider the ISAR images for the full-size car in Fig.3. The images show that the approximate dimensions of the car
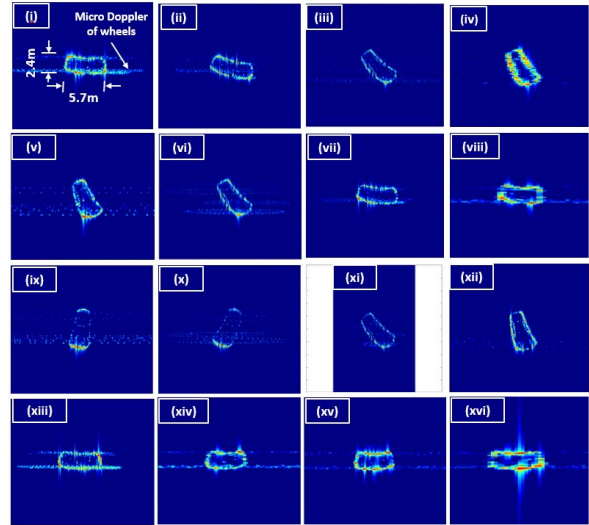

Fig. 3: ISAR images of full-size car at CPI corresponding to 1,2,3,4s carrying out (i-iv) right turn from west to south, (v-viii) left turn from north to east (ix-xii) U-turn from south to south and (xiii-xvi) straight path from east to west. The range span is 20m, while the cross-range span varies from 10m to 20m. The dynamic range is 20dB.

along the ground plane (5.7×2.4m) can be discerned from the range-cross range ambiguity plots. When the car is moving from the west to the south, the longer dimension of the car changes from the cross-range axis to the range axis from 1 to 4s. This conforms with the intuitive understanding of the orientation of the top- view of the target along its trajectory. Similarly, when the car turns left from north to east, the results show an initial image (at 1s) with the long dimension along the range to a final image (at 4s) with the long dimension along the cross-range. When a car is making a U-turn, the longer dimension is observed to always be along the range dimension. All the three turning motions that we have discussed so far have significant turning velocities. Interestingly enough, we get good quality ISAR images even for the fourth case when the car is moving along a straight trajectory from east to west. This is because of the change in the aspect of the car with respect to the radar along this trajectory.

241

As mentioned earlier, the simulations have incorporated the dynamics of the four wheels of the cars. The rotation of the wheels gives rise to micro-Dopplers, which cause distortions in the images as apparent in (i, ii, v, vi, ix, x, xiii, xiv) images. In some of the images, we observe four distinct micro-Doppler tracks corresponding to the four wheels of the vehicle. While the range span is fixed for all the images, the center of the range axis shifts based on the CRP (center of the vehicle) of the range window at the corresponding CPI. The cross-range spans are not fixed and are dependent on the angular velocity estimated from the target motion. Therefore, we note the image (xi) shows a smaller cross-range axis than the other images due to the high turning velocity during the U-turn motion.

Mid-size Car: The ISAR images of the mid-size car are presented in Fig.4. The results again show a fairly good estimate of the size of the

Fig. 5: ISAR images of the bicycle at CPI corresponding to 1,2,3,4s carrying out (i-iv) right turn from west to south, (v-viii) left turn from north to east (ix-xii) U-turn from south to south and (xiii-xvi) straight path from east to west. The range span is 20m, while the cross-range span varies from 10m to 20m. The dynamic range is 20dB.

the back of the vehicle due to its distinct shape and the micro-Doppler tracks from the wheels.
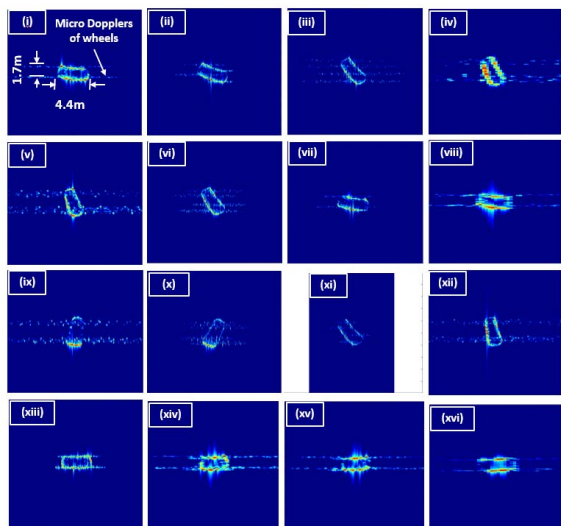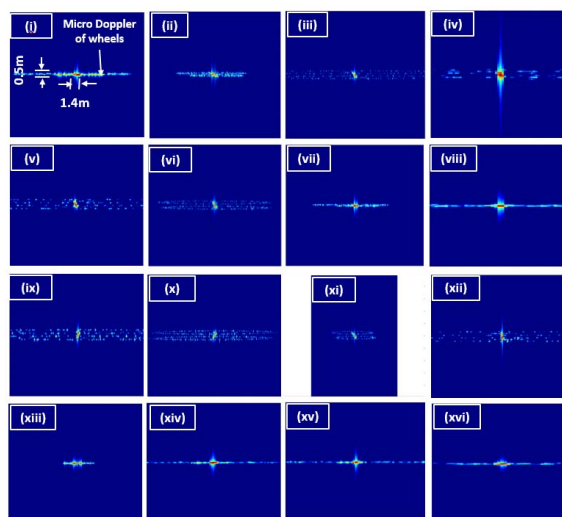

Fig. 4: ISAR images of mid-size car at CPI corresponding to 1,2,3,4s carrying out (i-iv) right turn from west to south, (v-viii) left turn from north to east (ix-xii) U-turn from south to south and (xiii-xvi) straight path from east to west. The range span is 20m, while the cross-range span varies from 10m to 20m. The dynamic range is 20dB.

vehicle - 4.4×1.7m - that may be useful for ATR. Also, based on the orientation of the vehicle in the images, we can learn to infer the type of trajectory undertaken by the car. The strong micro-Doppler returns from the wheels may provide additional information on the number of wheels of the vehicle, which may be useful for ATR purposes.

Bicylce: The ISAR images of the bicycle, shown in Fig.5, differ considerably from those of a car. First, since the vehicle is much smaller, the different point scatterers are not very well resolved and almost appear as a single point scatterer. The dimensions of the bicycle - especially its width - are much harder to discern from these images. Again, we observe micro-Doppler distortions from the two wheels of the bicycle. In our simulations, we did not model the rider on the bicycle. Hence the micro-Dopplers effects arising from the movements of the rider, such as the motion of his knees (while cycling) and hands while steering the wheels, are not captured in these images.

Auto-rickshaw: The auto-rickshaw is a three-wheeler, and its ISAR images are presented in Fig.6. The results clearly show the almost triangular shape of the top view of the vehicle providing a fairly good estimate of the dimensions of the vehicle. While moving in the transverse direction with respect to the radar (east to west or vice versa), the longer dimension of the auto-rickshaw is oriented along the cross-range. The image is reoriented with the longer dimension along with the range when the direction of the vehicle is longitudinal with respect to the radar. Interestingly, we can even observe the difference between the front and
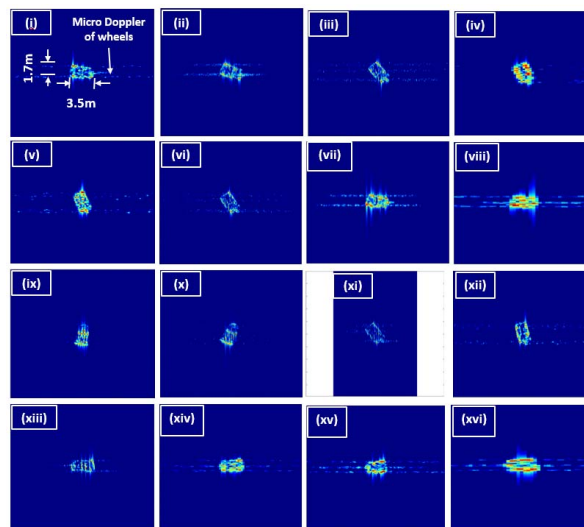

Fig. 6: ISAR images of auto-rickshaw at CPI corresponding to 1,2,3,4s carrying out (i-iv) right turn from west to south, (v-viii) left turn from north to east (ix-xii) U-turn from south to south and (xiii-xvi) straight path from east to west. The range span is 20m while the cross-range span varies from 10m to 20m. The dynamic range is 20dB.

Truck: The largest automotive target that we have considered is a truck whose ISAR images are shown in Fig.7. The size of the truck is estimated to be approximately 8.5×2.6m. Since the length of the truck is considerably larger than its width, it is fairly easy to discern the orientation of the vehicle with respect to the radar from the images. The truck has four wheels whose micro-Dopplers can be observed in some images. Larger trucks with a greater number of wheels will, most likely, give rise to more number of such micro-Doppler tracks in the images.
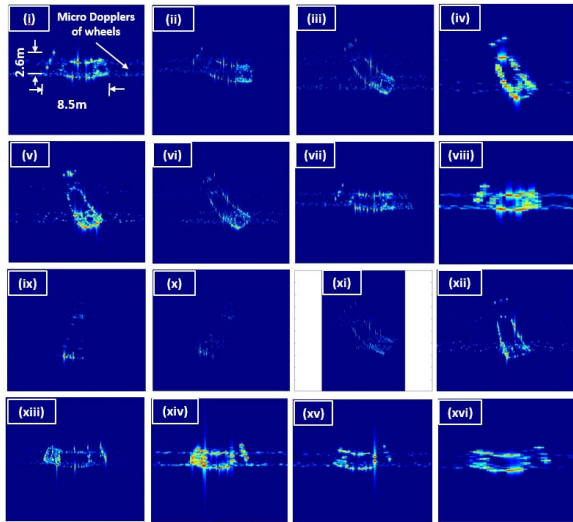
242

Fig. 7: ISAR images of truck at CPI corresponding to 1,2,3,4s carrying out (i-iv) right turn from west to south, (v-viii) left turn from north to east (ix-xii) U-turn from south to south and (xiii-xvi) straight path from east to west. The range span is 20m while the cross-range span varies from 10m to 20m. The dynamic range is 20dB.

V. CONCLUSION

We have provided an open-source database of simulated ISAR images of five common automotive targets along 16 distinct trajectories in a traffic junction. Broadband radar data were generated by integrating scattering center-based electromagnetic modeling with computer-animated dynamic targets. The radar returns are stretch processed along the fast time, and Fourier processed along the slow time to obtain range - cross-range ambiguity plots. The simulated radar images are idealized images free of noise and clutter artefacts as well as the effects of improper translational motion compensation. They provide very useful insights into the type of the target on the basis of the range and cross-range spans in the ambiguity plots; on the number of wheels in the vehicles on the basis of micro-Doppler tracks along the cross-range dimension; and the type of trajectory undertaken by the vehicle on the basis of the orientation of the image in the range cross-range space. Hence, we believe that these images can serve as useful training data for machine learning algorithms for automatic target recognition. Further, these models can be easily augmented to include real-world effects such as noise, clutter, and effects of errors in the parameter estimation.

REFERENCES

[1] K. Bengler, K. Dietmayer, B. Farber, M. Maurer, C. Stiller, and H. Winner, "Three decades of driver assistance systems: Review and future perspectives," *IEEE Intelligent Transportation Systems Magazine*, vol. 6, no. 4, pp. 6–22, winter 2014.

[2] J. Hasch, E. Topak, R. Schnabel, T. Zwick, R. Weigel, and C. Waldschmidt, "Millimeter-wave technology for automotive radar sensors in the 77 ghz frequency band," *IEEE Transactions on Microwave Theory and Techniques*, vol. 60, no. 3, pp. 845–860, 2012.

[3] V. C. Chen, *Inverse Synthetic Aperture Radar Imaging; Principles*. Institution of Engineering and Technology, 2014.

[4] T. Sauer and A. Schroth, "Robust range alignment algorithm via hough transform in an isar imaging system," *IEEE Transactions on Aerospace and Electronic Systems*, vol. 31, no. 3, pp. 1173–1177, 1995.

[5] D. L. Mensa, "High resolution radar cross-section imaging," *Boston, MA, Artech House, 1991, 280 p.*, 1991.

[6] C. Ozdemir, *Inverse synthetic aperture radar imaging with MATLAB algorithms*. John Wiley & Sons, 2012, vol. 210.

[7] M. Martorella, E. Giusti, A. Capria, F. Berizzi, and B. Bates, "Automatic target recognition by means of polarimetric isar images and neural networks," *IEEE Transactions on Geoscience and Remote Sensing*, vol. 47, no. 11, pp. 3786–3794, 2009.

[8] M. Vespe, C. Baker, and H. Griffiths, "Automatic target recognition using multi-diversity radar," *IET Radar, Sonar & Navigation*, vol. 1, no. 6, pp. 470–478, 2007.

[9] S.-H. Park, M.-G. Joo, and K.-T. Kim, "Construction of isar training database for automatic target recognition," *Journal of Electromagnetic Waves and Applications*, vol. 25, no. 11-12, pp. 1493–1503, 2011.

[10] M. Saidi, B. Hoeltzener, A. Toumi, A. Khecnhaf, and D. Aboutajdine, "Automatic recognition of isar images: Target shapes features extraction," in *2008 3rd International Conference on Information and Communication Technologies: From Theory to Applications*. IEEE, 2008, pp. 1–6.

[11] J. S. Kulpa, M. Malanowski, D. Gromek, P. Samczyńsk, K. Kulpa, and A. Gromek, "Experimental results of high-resolution isar imaging of ground-moving vehicles with a stationary fmcw radar," *International Journal of Electronics and Telecommunications*, vol. 59, no. 3, pp. 293–299, 2013.

[12] C. J. Li and H. Ling, "Wide-angle isar imaging of vehicles," in *2015 9th European Conference on Antennas and Propagation (EuCAP)*. IEEE, 2015, pp. 1–2.

[13] C. Li and H. Ling, "Wide-angle, ultra-wideband isar imaging of vehicles and drones," *Sensors*, vol. 18, no. 10, p. 3311, 2018.

[14] A. A. Danylov, T. M. Goyette, J. Waldman, M. J. Coulombe, A. J. Gatesman, R. H. Giles, X. Qian, N. Chandrayan, S. Vangala, K. Termkoa *et al.*, "Terahertz inverse synthetic aperture radar (isar) imaging with a quantum cascade laser transmitter," *Optics express*, vol. 18, no. 15, pp. 16 264–16 272, 2010.

[15] M. Boshra and B. Bhanu, "Bounding sar atr performance based on model similarity," in *Algorithms for Synthetic Aperture Radar Imagery VI*, vol. 3721. International Society for Optics and Photonics, 1999, pp. 716–729.

[16] H. Essen, M. Hagelen, W. Johannes, R. Sommer, A. Wahlen, M. Schlechtweg, and A. Tessmann, "High resolution millimetre wave measurement radars for ground based sar and isar imaging," in *2008 IEEE Radar Conference*. IEEE, 2008, pp. 1–5.

[17] G. Rubin, E. V. Sager, and D. H. Berger, "Gpu acceleration of sar/isar imaging algorithms," in *Antenna Measurement Techniques Association Symposium*, 2010, pp. 430–435.

[18] D. H. Nguyen, J. H. Kay, B. J. Orchard, and R. H. Whiting, "Classification and tracking of moving ground vehicles," *Lincoln Laboratory Journal*, vol. 13, no. 2, pp. 275–308, 2002.

[19] A. R. Brenner and J. H. Ender, "Very wideband radar imaging with the airborne sar sensor pamir," in *IGARSS 2003. 2003 IEEE International Geoscience and Remote Sensing Symposium. Proceedings (IEEE Cat. No. 03CH37477)*, vol. 1. IEEE, 2003, pp. 533–535.

[20] D. A. Morgan, "Deep convolutional neural networks for atr from sar imagery," in *Algorithms for Synthetic Aperture Radar Imagery XXII*, vol. 9475. International Society for Optics and Photonics, 2015, p. 94750F.

[21] S. A. Wagner, "Sar atr by a combination of convolutional neural network and support vector machines," *IEEE Transactions on Aerospace and Electronic Systems*, vol. 52, no. 6, pp. 2861–2872, 2016.

[22] O. Karabayır, O. M. Yücedağ, M. Z. Kartal, and H. A. Serim, "Convolutional neural networks-based ship target recognition using high resolution range profiles," in *2017 18th International Radar Symposium (IRS)*. IEEE, 2017, pp. 1–9.

[23] B. Xue and N. Tong, "Diod: Fast and efficient weakly semi-supervised deep complex isar object detection," *IEEE Transactions on Cybernetics*, 2018.

[24] G. Duggal, K. V. Mishra, and S. S. Ram, "Micro-doppler and micro-range detection via doppler-resilient 802.11ad-based vehicle-to-pedestrian radar," in *IEEE Radar Conference 2019*, 2019, pp. 1–6.

[25] K. V. Mishra, S. S. Ram, S. Vishwakarma, and G. Duggal, "Doppler-resilient 802.11 ad-based ultra-short range automotive radar," *arXiv preprint arXiv:1902.01306*, 2019.

[26] G. T. Ruck, D. E. Barrick, W. D. Stuart, and C. K. Krichbaum, *Radar cross section handbook*. Plenum press New York, 1970, vol. 1.